First-principles study of liquid and amorphous $InGeTe_2$

E. Spreafico,[1] S. Caravati,[2] and M. Bernasconi[1,*]

[1]*Dipartimento di Scienza dei Materiali, Università di Milano-Bicocca, Via R. Cozzi 53, I-20125 Milano, Italy*

[2]*Department of Chemistry and Applied Biosciences, ETH Zurich, USI Campus, Via Giuseppe Buffi 13, 6900 Lugano, Switzerland*

(Received 8 July 2010; revised manuscript received 11 February 2011; published 28 April 2011)

Based on *ab initio* molecular dynamics simulations, we generated models of liquid and amorphous $InGeTe_2$ of interest for applications in electronic data storage. The local geometry of Ge and Te atoms in amorphous $InGeTe_2$ is similar to that found in the extensively studied $Ge_2Sb_2Te_5$ and GeTe phase-change materials already exploited in nonvolatile memory applications. Atoms of In are instead mostly fourfold coordinated in $InTe_4$ tetrahedra, similar to the elementary units of crystalline InTe and In_2Te_5.

DOI: 10.1103/PhysRevB.83.144205 PACS number(s): 61.43.Fs, 61.43.Bn, 63.50.−x, 71.55.Jv

I. INTRODUCTION

Phase-change materials based on chalcogenide alloys are attracting increasing interest for applications in nonvolatile memories (phase-change memories; PCM) which exploit the large change in conductivity between a crystalline metallic phase and an insulating amorphous phase.[1–3] Although $Ge_2Sb_2Te_5$ (GST) is presently the material of choice for PCMs, chalcogenide alloys with different compositions are under scrutiny to improve PCM performances. To make PCM suitable for applications in automotive technologies, for instance, the stability of the amorphous phase against recrystallization must be extended above 125 °C, but still preserving a fast phase switching.[2] $InGeTe_2$ (IGT) has been recently proposed as a candidate for automotive use[4] since it reaches a crystallization temperature of 276 °C, about 130 °C higher than GST. It has been demonstrated that PCM devices based on IGT are able to reach 10 years' retention at temperatures higher than 150 °C.[4] A more recent work[5] showed that best performances are achieved in $(InTe)_x(GeTe)$ alloys with $x < 0.3$. Despite the potential technological interest of InGeTe alloys, information on their basic physical properties is very sparse. In this respect, *ab initio* simulations can provide insights on the structural and functional properties of phase-change materials for PCMs as demonstrated by recent work on several compounds, mostly along the pseudobinary $(GeTe)_x$-$(Sb_2Te_3)_y$ line[6–14] including the related binary systems GeTe[9,15] and Sb_2Te_3.[16]

In this paper, we investigate the properties of models of amorphous IGT generated by quenching from the melt by means of first-principles molecular dynamics simulations within the same framework used in our previous works on GST,[6–8] GeTe,[15] and Sb_2Te_3.[16]

II. COMPUTATIONAL DETAILS

The amorphous model was generated by quenching from the melt within *ab initio* molecular dynamics simulations by using the scheme of Kühne *et al.*[17] In the spirit of the Car-Parrinello (CP) approach the wave functions are not self-consistently optimized during the dynamics. However, in contrast to CP, large integration time steps can be used in the simulation. This scheme leads to a slightly dissipative dynamics of the type $-\gamma_D \dot{\mathbf{R}}_I$, where $\mathbf{R}_I$ are the ionic coordinates. In Ref. 17 it is shown how to compensate for this dissipation and obtain a correct canonical sampling. This scheme is implemented in the CP2K suite of programs.[18,19] We used the generalized gradient approximation (GGA) to the exchange-correlation functional as proposed by Perdew-Burke-Ernzerhof.[20] Goedecker-type pseudopotentials[21] with three, four, and six valence electrons were adopted for In, Ge, and Te, respectively. The Kohn-Sham (KS) orbitals were expanded in a triple-zeta-valence plus polarization Gaussian-type basis set and the charge density was expanded in a plane-wave basis set with a cutoff of 100 Ry to efficiently solve the Poisson equation within the Quickstep scheme.[18,19] Brillouin zone integration was restricted to the supercell Γ point. A time step of 2 fs was used. For a 216-atom supercell, we observed a speedup by a factor of 25 with respect to standard Born-Oppenheimer simulations with the CP2K code and a similar speedup with respect to CP simulations with the CPMD code[22] and a time step of 0.2 fs. In the case of liquid GST, extensive tests have been performed on the validity of the scheme of Ref. 17 by computing structural and dynamical properties at the melting point by means of standard Born-Oppenheimer simulations which yielded undistinguishable results on pair correlation functions (on the scale of Fig. 1) and the same self-diffusion coefficient within a few percent.[6] To correctly reproduce the band gap, electronic densities of states were calculated from KS energies with the HSE03 hybrid functional[23] on geometries optimized with the less computationally demanding Perdew-Burke-Ernzerhof functional.

IGT is known to crystallize in a face-centered-cubic (fcc) structure with lattice parameter $a = 6.02$ Å,[24] a value very close to that of GST, which crystallizes in a rock-salt geometry, with Te fully occupying one sublattice and Ge, Sb, and 20% of vacancies randomly distributed on the other sublattice.[25] Although the stoichiometry of IGT is compatible with an ideal rock-salt structure, the measured experimental density of IGT ($\rho_c = 0.0316$ atom/Å^3)[26] is 16% lower than that expected for a rock-salt crystal with a measured lattice parameter of 6.02 Å (0.0367 atom/Å^3). One possible explanation for this inconsistency might invoke the presence of vacancies on both the (In,Ge) and the Te sublattices. Since we are not aware of experimental data on the density of the liquid phase, we proceeded as follows. We considered a cubic supercell with edge 18.06 Å long, with 216 atoms arranged in the rock-salt geometry with Te atoms on a sublattice and In and Ge randomly distributed on the other sublattice at the

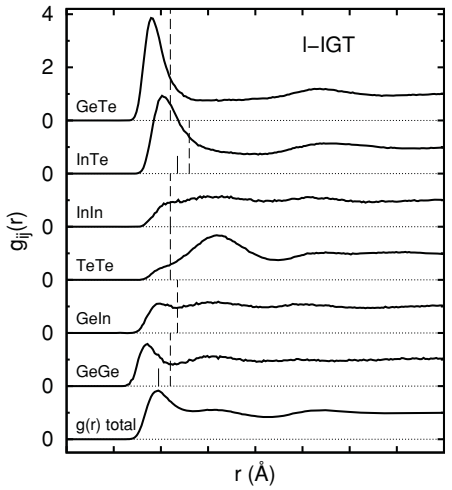

FIG. 1. Total and partial pair correlation functions of l-IGT. The first maximum is at position 2.811 Å (Ge-Te), 3.053 Å (In-Te), and 2.701 Å (Ge-Ge). Long vertical lines indicate the bonding cutoff used to define coordination numbers; shorter vertical lines indicate the bonding cutoff defined for amorphous IGT (cf. Fig. 5).

density of the ideal rock-salt phase (0.0367 atom/Å^3). Then the crystal was molten at a fixed density, equilibrated for 5 ps at 2500 K, quenched in 10 ps, and further equilibrated for 25 ps at 1050 K, close to the experimental melting temperature (at normal pressure).[4] The system was then equilibrated at 1050 K at several lower densities (for 20 ps each) by rescaling the edge of the cubic supercell. The calculated pressure-versus-volume isotherm was then extrapolated to estimate the equilibrium density at zero pressure. To this aim we added to the *ab initio* pressure the contribution from van der Waals (vdW) interaction following the scheme proposed by Grimme.[27] The resulting theoretical equilibrium density of IGT is 0.0303 atom/Å^3, which is, however, subject to large uncertainties due to the approximation involved in the semiempirical description of vdW interactions. Unfortunately, no experimental data on the density of the liquid is available to assess these approximations for IGT. However, by applying the same procedure to liquid GeTe,[15] we obtained an equilibrium density 7% lower than in experiments. At the theoretical equilibrium density the contribution of the vdW interaction to the pressure is 15 GPa in GeTe and 2 GPa in IGT. We remark that in the absence of semiempirical vdW interaction, the equilibrium density of liquid GeTe is much lower than in experiments, with a misfit larger than 20%. The equilibrium density of the solid is instead much better reproduced also without vdW correction. For GST, for instance, the theoretical density of the cubic phase is only 6% lower than in experiments.[8]

The analysis of structural and electronic properties of the liquid at the theoretical equilibrium density of 0.0303 atom/Å^3 at 1050 K is discussed in Sec. III A. To generate a model of a-IGT the liquid was brought to 300 K in 60 ps. Because of the uncertainties in the theoretical equilibrium density of the liquid, we generated amorphous models by quenching from the melt at different densities. The theoretical equilibrium density of the amorphous models was then computed from a Murnaghan fitting of the energy-volume data for the optimized geometries at fixed volume at zero temperature. The equilibrium density of the amorphous phase changes by less than 2% by changing the density of the liquid in the wide range of 0.0367–0.0279 atom/Å^3. The model of a-IGT at the theoretical equilibrium density of 0.0283 atom/Å^3 was then equilibrated at 300 K for 50 ps.

III. RESULTS

A. Liquid phase

The pair correlation functions of the liquid phase (l-IGT) at 1050 K at the estimated theoretical density (0.0303 atom/Å^3; cf. Sec. II) are reported in Fig. 1, while the angle distribution function is reported in Fig. 2 with the distribution of coordination numbers.

The average coordination numbers are obtained by integrating the partial correlation functions up to a given cutoff which is customarily assigned by the first minimum in the pair correlation functions. In l-IGT the first minimum is well defined only for the Ge-Ge pair. To assign the coordination numbers, we considered two sets of cutoff distances: one corresponding to those of our model of amorphous IGT discussed in Sec. III B and the second one assigned as in Fig. 1. The resulting average coordination numbers are listed in Table I for the two sets of cutoff distances.

A large fraction of wrong bonds, that is, different from the Ge-Te and In-Te bonds expected in the rock-salt crystal,

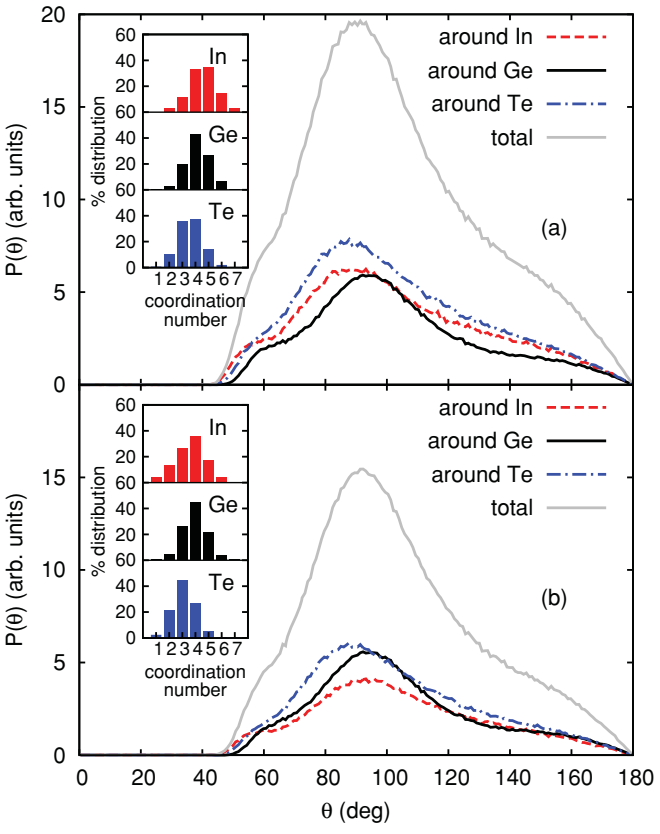

FIG. 2. (Color online) Angle distribution functions of l-IGT for the bonding cutoff of (a) the liquid phase (cf. Fig. 1) and (b) the amorphous phase (cf. Fig. 5). Insets: Distribution of coordination numbers of the different species.

TABLE I. Average coordination number for different pairs of atoms in l-IGT computed from the partial pair correlation functions. Data for l-IGT with the bonding cutoff of a-IGT (see text) are given in parentheses.

	With In	With Ge	With Te	Total
In	0.273 (0.273)	0.604 (0.604)	3.674 (2.711)	4.552 (3.589)
Ge	0.604 (0.604)	0.681 (0.470)	2.867 (2.867)	4.152 (3.941)
Te	1.837 (1.356)	1.433 (1.433)	0.327 (0.327)	3.598 (3.116)

are present in l-IGT. Still, In and Ge are preferentially bonded with Te, the most common configurations being Ge-Te_3, Ge-$GeTe_3$, In-Te_4, and In-Te_3. The angle distribution function (Fig. 2) displays broad peaks at $\sim 90^\circ$ and $\sim 170^\circ$ that indicate the presence of an octahedral-like geometry similar to that of the crystalline phase. The shoulder at $\sim 60^\circ$ is due to the presence of three-membered rings. The ring distribution is reported in the inset in Fig. 3 as averaged over 50 configurations of the liquid. The four-membered ring is the most abundant, as in GST and related binary materials.[6,8,9,11,15,16]

The calculated x-ray- and neutron-weighted total scattering functions $S(Q)$ of l-IGT are reported in Fig. 3 for future reference since experimental scattering data are presently not available. From the analysis of the structure factor of several chalcogenide liquids, it was proposed[29] that the ratio between the heights of the first two peaks of $S(Q)$ is an indicator of the local bonding geometry. Namely, the quantity $S = S(Q_2)/S(Q_1)$, where Q_1 and Q_2 are the positions of the first two peaks of the structure factor, is >1 for a tetrahedral liquid and <1 for an octahedral liquid. Our model of l-IGT is an octahedral liquid, and indeed $S < 1$, which further confirms the correlation proposed in Ref. 29.

Note the presence of a small peak at ~ 1 Å^{-1} in the neutron-weighted $S(Q)$, which is mostly due to the partial Ge-Te correlation function, whose contribution is reduced in the x-ray-weighted $S(Q)$ because of the lower nuclear

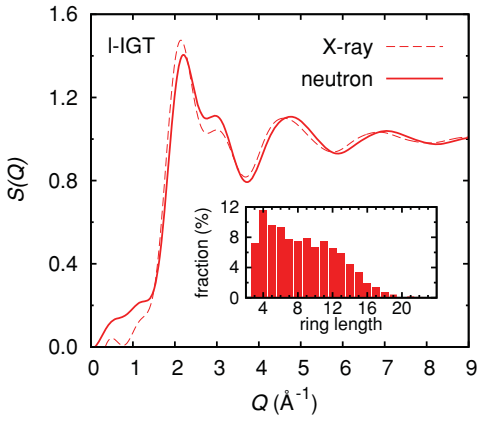

FIG. 3. (Color online) The x-ray-weighted (dashed line; according to Eq. (56) in Ref. 28 with the Q-dependent x-ray atomic form factors) and neutron-weighted (Eq. (20) in Ref. 28) total scattering function $S(Q)$ of l-IGT at 1050 K. Inset: Ring distribution function of l-IGT computed as in Ref. 31. For sake of comparison with the amorphous phase, the bonding cutoff of a-IGT is used (cf. Fig. 1).

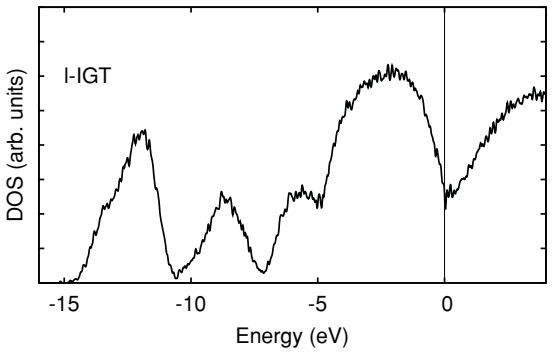

FIG. 4. Electronic density of states of l-IGT at the HSE03 level averaged over 58 configurations in the liquid phase at 1050 K. The Kohn-Sham energies are broadened with Gaussian functions 27 meV wide. The zero of energy corresponds to the Fermi level.

charge of Ge with respect to the other species. A similar first diffraction peak at low Q is present in the neutron-weighted $S(Q)$ of liquid and amorphous GST.[8] The first diffraction peak at low Q in liquid and amorphous selenides and oxides has been the subject of extensive investigation over the years, which assigned this feature to the presence of structural units responsible for intermediate-range order.[30] A discussion of the microscopic origin of the first diffraction peak in phase-change materials is postponed to a future publication.

The liquid is metallic with a high density of states (DOS) at the Fermi level as shown in Fig. 4.

B. Amorphous phase

1. *Structural properties*

The theoretical equilibrium density of the amorphous phase was computed from a Murnaghan fitting of the energy-volume data for the optimized geometries at zero temperature. The

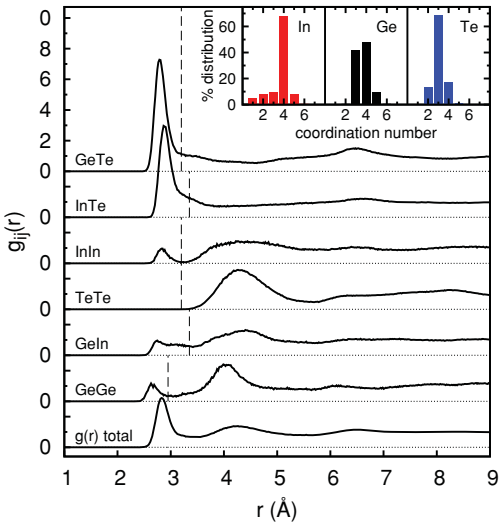

FIG. 5. (Color online) Total and partial pair correlation functions of a-IGT. The first maximum is at position 2.789 Å (Ge-Te), 2.875 Å (In-Te), 2.638 Å (Ge-Ge), and 2.727 Å (In-Ge). Vertical lines indicate the bonding cutoff used to define coordination numbers (see text). Inset: Distribution of coordination numbers of the different species.

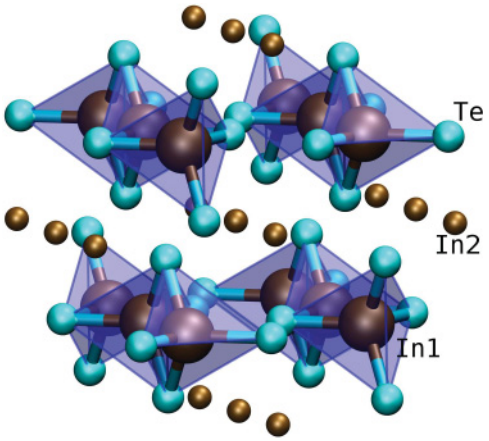

FIG. 6. (Color online) Crystal structure of InTe.[32] In1 atoms are at the center of edge-sharing $InTe_4$ tetrahedra forming chains aligned along the c axis. In2 atoms are weakly bound 3.576 Å from the Te atoms of the neighboring chains. Atoms of In are depicted by small and large dark (brown) spheres; Te atoms, by gray (light-blue) spheres.

theoretical equilibrium density of a-IGT is $\rho_a = 0.0283$ atom/Å^3. The density lowering in the crystalline-to-amorphous transition is $(\rho_c - \rho_a)/\rho_c \sim 4\%$ (6.4% in GST).[29] The calculated bulk modulus and derivative of the bulk modulus with respect to pressure are 11.8 GPa and 6.6, respectively. Previous calculations on GST and GeTe[8] revealed that GGA functionals underestimate bulk moduli and equilibrium densities. We are not aware of experimental data on the density of a-IGT.

The pair correlation functions are reported in Fig. 5. To assign the coordination numbers one usually integrates the pair correlation functions up to a distance cutoff taken as the position of the first minimum. However, in the case of In-Te and In-Ge bonds the first minimum is not well defined. This is due to the presence in the amorphous phase of weakly bonded In atoms similar to those present in the InTe crystal depicted in Fig. 6. In fact, in the tetragonal $I4/mcm$ phase of InTe, one recognizes two types of In atoms:[32] In1 at the center of edge-sharing $InTe_4$ tetrahedra forming chains and weakly bound In2 atoms between neighboring chains. In1-Te and In2-Te bond lengths are, respectively, 2.819 and 3.576 Å. Therefore, we chose as a bonding cutoff for In-Te in a-IGT the well-defined minimum of the pair correlation function of In-Te pairs in tetrahedra shown in Fig. 7. The fraction of tetrahedral In is weakly dependent on the choice of the cutoff to define the first coordination shell. Further discussion of this choice is given later by discussing the nature of chemical bonding in a-IGT.

TABLE II. Average coordination number for different pairs of atoms computed from the partial pair correlation functions (cf. Fig. 5) for a-IGT.

	With In	With Ge	With Te	Total
In	0.184	0.413	3.047	3.643
Ge	0.413	0.203	3.061	3.677
Te	1.523	1.531	–	3.054

Average coordination numbers for the different species are listed in Table II and the distribution of coordination numbers is reported in the inset in Fig. 5. Similarly to a-GST,[6,8] Ge atoms are mostly 4-coordinated and Te atoms are mostly 3-coordinated. However, the fraction of Ge atoms threefold coordinated is much larger in a-IGT than in a-GST[6,8] and a-GeTe.[10,15] Although In and Ge form bonds preferentially with Te atoms, we observed a large fraction of "wrong" Ge-Ge, In-Ge bonds, although smaller than in the liquid phase. As opposed to what found in *ab initio* models of a-GST[6] and a-GeTe,[15] Te-Te bonds are absent in a-IGT. The distribution of different environments of In, Ge, and Te in a-IGT is reported in Table III (Appendix). In and Ge are preferentially bonded with Te, the most common configurations being Ge-Te_4, Ge-Te_3, Ge-$InTe_3$, In-Te_3, In-$GeTe_3$, and In-Te_4. Nearly 50% of Ge and In atoms are bound at least to another Ge or In atom, and this fraction increases to 72% for 4-coordinated Ge.

Insight on the local geometry of a-IGT is gained from the angle distribution function in Fig. 8. The broad peak at $\sim 90^\circ$ and the weaker structure around $\sim 170^\circ$ for Ge are reminiscent of the octahedral-like geometry of the crystalline phase. For Te, only angles at $\sim 90^\circ$ are found. However, the main coordination of Ge and Te of 4 and 3, respectively, is

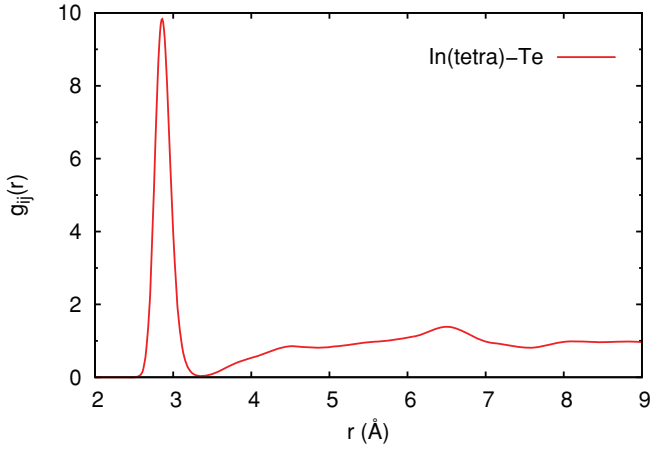

FIG. 7. (Color online) In-Te partial pair correlation function only for In in tetrahedra (see text). The maximum is at 2.859 Å.

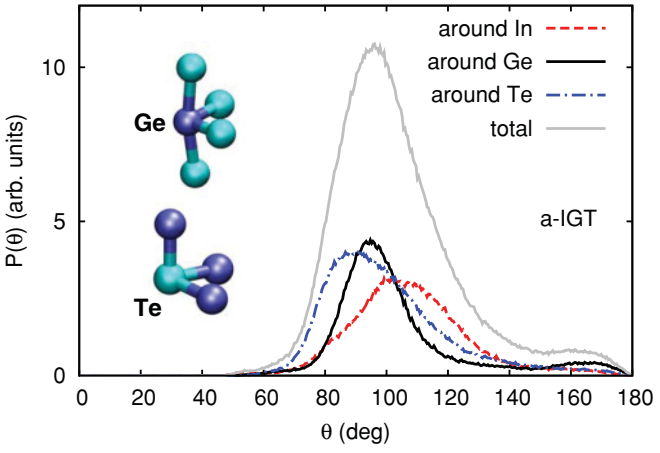

FIG. 8. (Color online) Angle distribution function of a-IGT. Inset: Defective octahedral environment for Ge and Te.

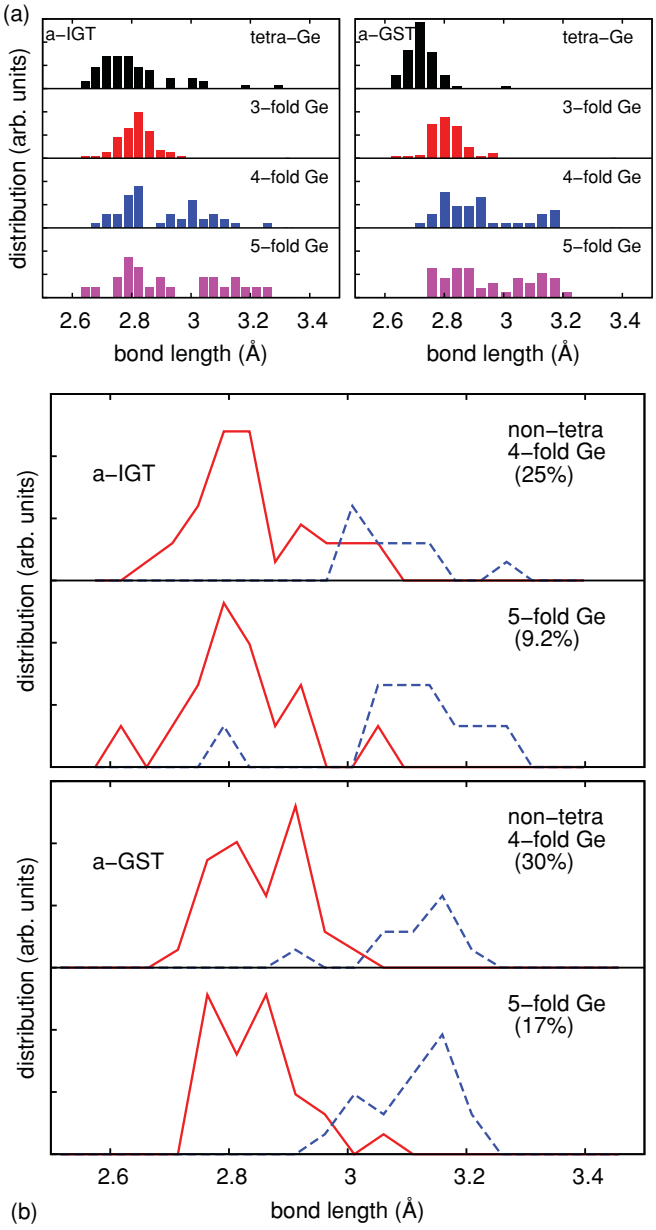

FIG. 9. (Color online) (a) Distribution of bond lengths for Ge in tetrahedral and defective octahedral sites with different coordinations. The same distributions for our model of a-GST presented in Ref. 6 are shown for sake of comparison. (b) Distribution of the three shorter (solid line) and the other, longer (dashed) bond lengths for Ge in defective octahedral sites with different coordinations.

lower than the ideal octahedral value of 6. In our model, and similarly to a-GST, a-GeTe, and a-Sb_2Te_3,[6,8,9,15,16] the presence of neighboring vacancies is responsible for the lower coordination, while the bonding angles remain close to $\sim 90^\circ$ and $\sim 180^\circ$ as in the crystalline phase.

Te and Ge in defective octahedral environments are depicted in the inset in Fig. 8. As in a-GST and a-GeTe, the majority of Ge atoms in a-IGT is in a defective octahedral environment mostly with coordination 4.[6,15] Actually, the distribution of the bond lengths for Ge atoms in octahedral-like sites reported in Fig. 9(a) shows a bimodal distribution which becomes more evident in Fig. 9(b), where the distribution is plotted for the three shorter bonds and for the longer ones. The defective octahedral-like environment of Ge recalls a $3+n$ ($n = 0$–2) geometry similar to the $3+3$ bonding coordination in crystalline α-GeTe.[36] Similar local structures are found in a-GST as shown by the bond length distributions reported for sake of comparison in Fig. 9. These structures are ruled by the formation of p bonds as pointed out by Xu *et al.*[37] and discussed further later on.

A fraction of 4-coordinated Ge atoms are in a tetrahedral environment. The average bond length of Ge is slightly shorter in tetrahedral sites than in defective octahedral sites (cf. Fig. 9). As already mentioned, also the majority of In atoms in a-IGT are in a tetrahedral geometry as already revealed by the broad peak of the angles distribution of In (Fig. 8) which is shifted toward the tetrahedral value of $\sim 109.5^\circ$. To highlight the presence of atoms in a tetrahedral geometry, we considered the local order parameter q used in Ref. 6. q is defined by $q = \frac{1}{3} - \frac{3}{8}\sum_{i>k}(\frac{1}{3} + \cos\theta_{ijk})^2$, where the sum runs over the couples of atoms bonded to a central atom j. $q = 1$ for the ideal tetrahedral geometry, $q = 0$ for the six-coordinated octahedral site, and $q = 5/8$ for a 4-coordinated defective octahedral site. The distribution of the local order parameter q for Te, Ge, and In atoms is reported in Fig. 10 for different coordination numbers. The q distribution for Te shows no signature of the tetrahedral geometry. The q distribution for 4-coordinated Ge is further analyzed in terms of atoms bonded to Te only or to at least one Ge or In (Fig. 10). The latter distribution reveals a bimodal shape, with two structures corresponding to the defective octahedra and tetrahedra. The presence of wrong bonds (Ge-Ge and In-Ge) clearly favors the tetrahedral geometry around Ge. The q distribution of 4-coordinated In shows only the tetrahedral peak, with a low tail at the octahedral value. A very large fraction of In

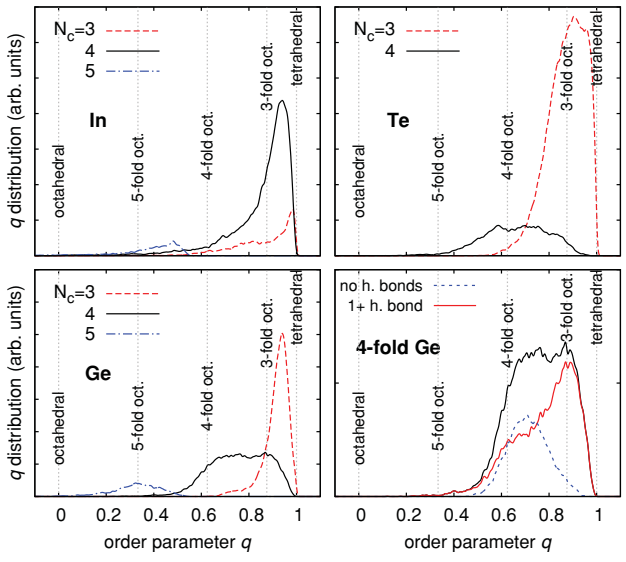

FIG. 10. (Color online) Distribution of the local order parameter q (see text) for Te, Ge, and In in a-IGT. Vertical lines indicate the values of q for selected ideal geometries. N_c indicates the coordination number. In the lower right panel the q distribution of 4-coordinated Ge is further resolved for Ge with at least one wrong bond (with Ge or In) or bonding with Te only (no homopolar bonds).

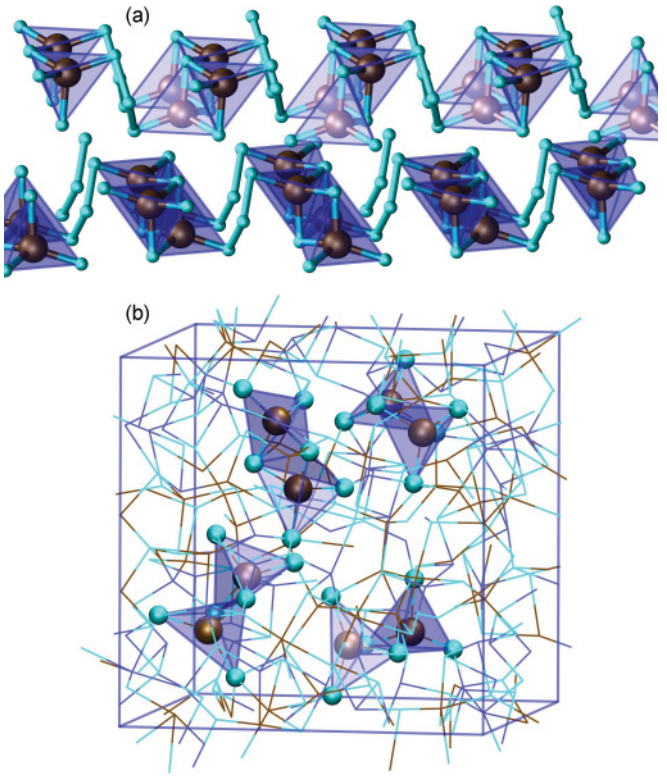

FIG. 11. (Color online) (a) Structure of crystalline In_2Te_5 made of chains of edge-sharing $InTe_4$ tetrahedra interlinked via Te trimers.[42] (b) Arrangement of $InTe_4$ edge-sharing tetrahedra in a-IGT. Atoms of In are depicted by large dark (brown) spheres; Te atoms, by gray (light-blue) spheres.

atoms is thus in a tetrahedral geometry. Due to the broad features of the q distribution, we quantified the number of atoms in tetrahedral geometry from the analysis of the Wannier functions as discussed later. The presence of In in tetrahedral geometry is not surprising if we consider that $InTe_4$ tetrahedra are the elemental structural units of crystalline InTe (Fig. 6) and In_2Te_5 [Fig. 11(a)].[42] In the crystalline phases $InTe_4$ tetrahedra are edge-sharing forming chains. In In_2Te_5 the chains are interlinked via Te trimers [Fig. 11(a)], while in InTe, weakly bound In atoms are present between neighboring chains. In a-IGT, 28% of $InTe_4$ tetrahedra are edge-sharing similarly to the crystal, as depicted in Fig. 11(b), the other tetrahedra being corner-sharing (41%) or isolated (17%).

Regarding the medium-range order in a-IGT, we report the ring distribution in Fig. 12. As occurs in a-GST, the four-membered ring is the most abundant among the smaller rings. A large fraction of four-membered rings (87%) is made by ABAB rings (A = In, Ge and B = Te) without homopolar bonds. Note that here four-membered rings correspond to both the square rings typical of the rock-salt structure and to those originating from the edge-sharing $InTe_4$ tetrahedra. One notes the presence of very large rings, which indicates that a-IGT has a structure more open than that of a-GST.[6,16]

2. *Chemical bonding*

Insight on the chemical bonding and oxidation state of the different species can be obtained from Bader charges computed

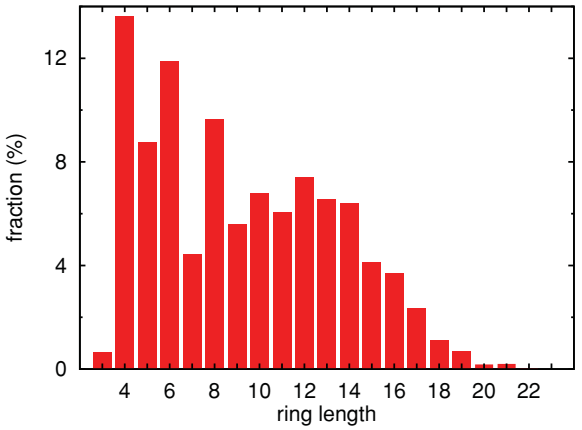

FIG. 12. (Color online) Ring distribution function of a-IGT computed as in Ref. 31.

according to the scheme of Ref. 33 and from Wannier functions (WFs) computed as in Refs. 34 and 35.

The Bader charges of a-IGT are given in Fig. 13. The Bader charges of In in crystalline InTe are also reported as horizontal lines in Fig. 13, as computed in a relaxed InTe supercell (192 atoms) at the experimental lattice parameters.[32] The formal charges of two In species in InTe, In1 and In2, can be assigned to +3 and +1 for a closed-shell system. The presence of two oxidation states for In in crystalline InTe is confirmed by the two values of the Bader charges in Fig. 13. The charges of In in a-IGT have a bimodal distribution centered at the values found in the crystal. Due to the presence of In-Ge and In-In bonds in a-IGT, it is not possible to uniquely assign the lower charges to weakly bonded In atoms as in the crystal. However, the charges of In atoms in tetrahedra not containing In-Ge and In-In bonds actually fall in the upper peak of the bimodal distribution in Fig. 13. By inspection of the Bader ionic charges, highly charged defects such as valence alternation pair states[43] are not found, similarly to what occurs in our models of a-GST, a-GeTe, and a-Sb_2Te_3,[6,8,15,16] possibly due to the lack of Te chains.

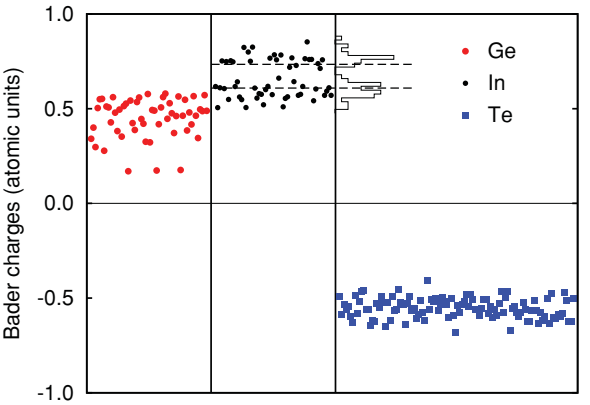

FIG. 13. (Color online) Bader ionic charges (atomic units) of the model of a-IGT. Each point corresponds to an individual atom in the 216-atom supercell. Dashed horizontal lines correspond to the charge of In1 and In2 atoms in crystalline InTe (see text). The distribution of In charges in a-IGT is also shown as a histogram.

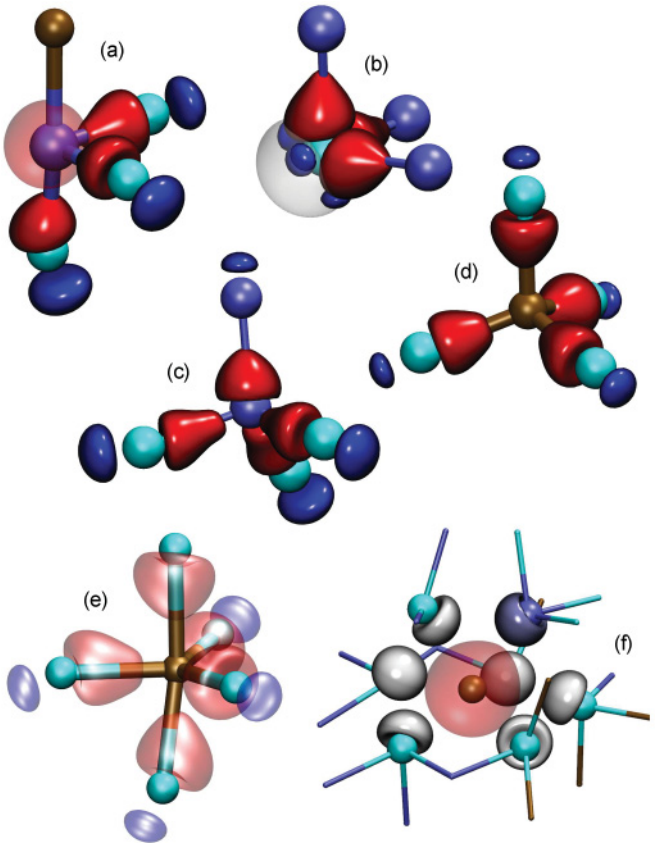

FIG. 14. (Color online) Isosurface of Wannier functions for (a) Ge in defective octahedra, (b) threefold-coordinated Te bonded to Ge, (c) Ge in tetrahedral sites, (d) In in $InTe_4$ tetrahedra, (e) fivefold-coordinated In, and (f) weakly bound In atoms. Atoms of In are depicted by small dark (brown) spheres, Ge by large dark (blue) spheres, and Te by gray (light-blue) spheres. Isosurfaces with different colors (red and blue) have different sign. Wannier functions with spherical isosurfaces are *s*-type lone pairs.

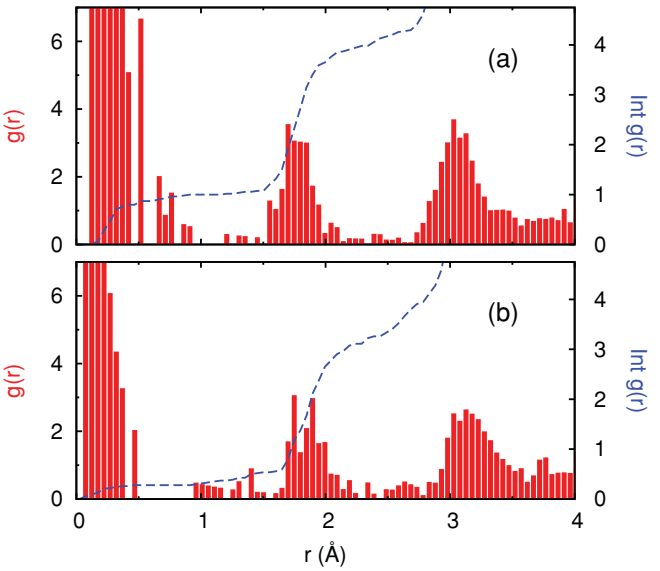

FIG. 15. (Color online) Pair correlation functions of (a) Ge or (b) In with the centers of Wannier functions. The dashed line is the running integral of the pair correlation function (right scale).

WFs offer a better description of the different bonding states of In and of other species as well. WFs are the periodic version of the Boys orbitals obtained by the unitary transformation of the Kohn-Sham occupied orbitals, which minimizes the quadratic spread.[34,35] Isosurfaces of the WF in the different bonding geometries are given in Fig. 14. For Ge in defective octahedra [Fig. 14(a)], one recognizes one *s*-type WF localized on Ge, which corresponds to an *s*-like lone pair, while the other three WFs are along the three shorter Ge-Te bonds. This analysis, however, does not exclude the presence of a weaker fourth bond along the longer Ge-Te bond resonating with the shorter one as the fourth bond is at a precise octahedral-like angular position. Its presence cannot be accidental and assigned to a second shell of neighbors. In this respect, the bonding coordination of 3 assigned to Ge by the analysis of WFs given above and by the electron localization function (ELF) in Ref. 37 is incomplete. In the presence of the (partially) resonating valence bonds proposed in Refs. 38 and 39, the WFs do not convey a full description of the bonding. The WFs of benzene, for instance, just display one of the Keluké structures, and not the resonating π bonds.[40] Still, the WFs for Ge in defective octahedra clearly show a *p*-type bonding and an *s*-type lone pair. The same is true for Te, which displays three *p*-type WFs along the three bonds and an *s*-type lone pair [cf. Fig. 14(b)]. One of the three WFs actually corresponds to a dative bond to Ge. In defective octahedral sites Ge is divalent and needs a dative bond from a lone pair of Te to complete the *p* shell.[37] Ge in tetrahedra instead shows four sp^3-like WF along the four bonds [cf. Fig. 14(c)]. One can understand why wrong bonds, Ge-Ge or Ge-In in a-IGT, promote the formation of tetrahedral bonding of Ge as follows: in the absence of Te lone pairs due to the presence of wrong bonds, Ge cannot complete the *p* shell and then *s* electrons are promoted to the valence forming sp^3 hybrids and turning defective octahedra into tetrahedra. The same analysis of WFs applies to GST and GeTe.[6,8,15,16] It is actually possible to quantify the number of Ge in defective octahedra by counting the number of Ge atoms displaying an *s*-type WF localized on the atom. This can be achieved by integrating the correlation function between Ge atoms and the center of WF up to the first minimum (0.6 Å) given in Fig. 15. The average coordination number of Ge atoms with the WF localized on Ge multiplied by the total number of Ge atoms gives the number of Ge atoms with *s*-type lone pairs corresponding to Ge in defective octahedra. The resulting fraction of Ge in defective octahedra is 87%. The remaining 13% of Ge are in tetrahedra with a high value of the *q* parameter. Turning to In, in the tetrahedral sites four WFs along the bonds are recognizable [Fig. 14(d)]. By direct inspection of the WFs we count 63% of In in a tetrahedral configuration. The few (5 of 54 atoms; ~9%) fivefold-coordinated In atoms display three WFs typical of an sp^2 configuration, with additional WFs along the p_z orbitals [Fig. 14(e)]. The remaining In atoms (28%) are weakly bound, displaying an *s*-type spherical WF corresponding to a lone pair strongly localized on the atom [Fig. 14(f)].

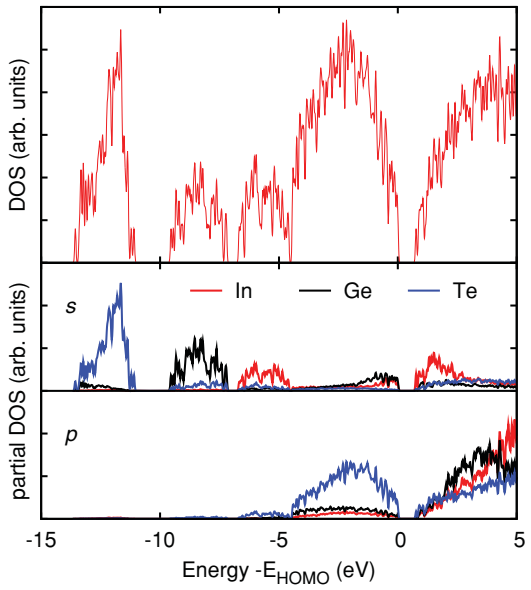

FIG. 16. (Color online) Electronic density of states of a-IGT. Projections of the DOS on atomic s and p pseudo–wave functions are also given. The contribution from d pseudo–wave functions is negligible on the scale of the figure and it is omitted. The zero of energy corresponds to the top of the valence band. The Kohn-Sham energies of a-IGT are broadened with Gaussian functions 27 meV wide (responsible for the small DOS above 0 eV).

3. *Electronic properties*

The electronic DOS of a-IGT is reported in Fig. 16 as computed from KS energies at the supercell Γ point with the HSE03 functional, broadened with a Gaussian function with variance of 27 meV. Projection of the DOS on atomic orbitals is also given in Fig. 16. While l-IGT is metallic (cf. Fig. 4), our a-IGT model is semiconducting, with a gap 0.5 eV large. To quantify the localization properties of individual KS states, we have computed the inverse participation ratio (IPR), which is defined for the ith KS state by $\sum_j c_{ij}^4/(\sum_j c_{ij}^2)^2$, where j runs over the Gaussian-type orbitals (GTOs) of the basis set and c_{ij} are the expansion coefficients of the i-th KS state in Gaussian-type orbitals. IPRs are given in Fig. 17. Few states at the conduction band edge are strongly localized, due to disorder. Strongly localized s-type states are present also deeper in energy.

The imaginary parts of the dielectric function ϵ_2 of a-IGT and a-GST are compared in Fig. 18. ϵ_2 is computed in the random phase approximation from KS orbitals as discussed in Ref. 41. Since the structure of crystalline IGT is not fully understood (see Sec. II), we cannot assess the optical contrast between the crystal and the amorphous phases.

4. *Vibrational properties*

We computed the phonon frequencies of a-IGT by diagonalizing the dynamical matrix, obtained in turn from the variation of atomic forces due to finite atomic displacements 0.0053 Å large. Only phonons with the periodicity of our supercell (Γ-point phonons) were considered. The phonon DOS of a-IGT and its projection on different species (In, Ge, and Te) are shown in Fig. 19. In an amorphous material,

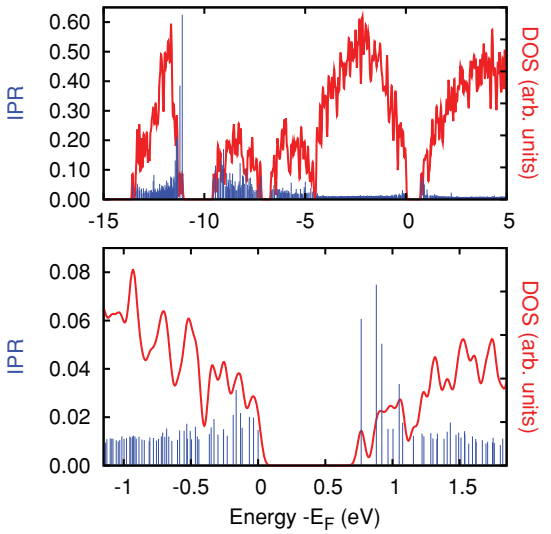

FIG. 17. (Color online) Electronic density of states of a-IGT and the corresponding values of the inverse participation ratio (IPR) (blue spikes, left scale; see text for definition). The zero of energy corresponds to the top of the valence band. A zooming of the DOS close to the band gap is shown in the lower panel. The Kohn-Sham energies are broadened with Gaussian functions 27 meV wide (responsible for the small DOS above 0 eV).

phonons display localization properties which depend on frequency. To address this issue, we have computed the IPR of the jth vibrational mode defined as

$$\mathrm{IPR} = \frac{\sum_\kappa \left| \frac{\mathbf{e}(j,\kappa)}{\sqrt{M_\kappa}} \right|^4}{\left(\sum_\kappa \frac{|\mathbf{e}(j,\kappa)|^2}{M_\kappa} \right)^2}, \tag{1}$$

where $\mathbf{e}(j,\kappa)$ are phonon eigenvectors and the sum over κ runs over the N atoms in the unit cell with masses M_κ. According to this definition, the value of IPR varies from $1/N$ for a completely delocalized phonon to one for a mode completely localized on a single atom (cf. Fig. 19).

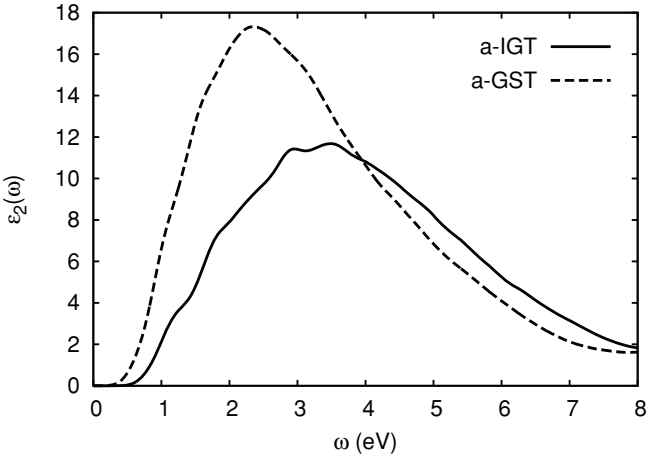

FIG. 18. Imaginary part of the dielectric function (ϵ_2) of amorphous IGT (solid lines) and GST (dashed lines, from Ref. 41).

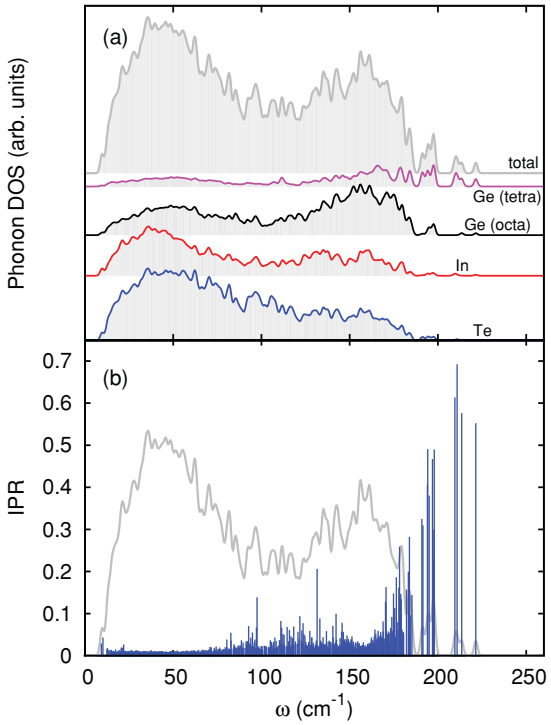

FIG. 19. (Color online) (a) Phonon density of states (DOS) of a-IGT and its projections on different species (In, defective octahedral and tetrahedral Ge, and Te). (b) Inverse participation ratio (IPR) for phonons in a-IGT (blue spikes, left scale; see text for definition) superimposed on the DOS.

The DOS is very similar to that of a-GST,[8] with a high-frequency tail due to modes mostly localized on Ge atoms in tetrahedral sites (cf. Fig. 19). Signatures of high-energy modes localized on tetrahedral Ge have been identified in the Raman spectrum of a-GeTe in our recent work.[15] Since In and Sb have similar masses, the projection of the DOS of a-GST on Sb is similar to the projection of the DOS of a-IGT on In.

From the projected DOS we also computed the Debye-Waller factor for each species, defined by[44]

$$B_\kappa = \frac{8\pi^2}{3}\langle \mathbf{u}_\kappa^2 \rangle,$$

where κ runs over the three species and $\langle \mathbf{u}_\kappa^2 \rangle$ is the mean average square displacement of atoms of species κ computed from harmonic phonons as

$$\langle \mathbf{u}_\kappa^2 \rangle = \frac{1}{N_\kappa} \sum_{j,m} \frac{\hbar}{\omega_j} \frac{|\mathbf{e}(j,m)|^2}{M_\kappa} \left[n_B\left(\frac{\hbar\omega_j}{k_B T}\right) + \frac{1}{2} \right], \qquad (2)$$

where m runs over N_κ atoms of species κ, and ω_j and $\mathbf{e}(j,m)$ are the frequency and eigenvector of the jth harmonic phonon. The temperature dependence is introduced by the Bose factor $n_B(\frac{\hbar\omega_j}{k_B T})$. The resulting Debye-Waller factors as a function of temperature, reported in Fig. 20, are similar to those we have previously computed for a-GST.[8] The large Debye-Waller factor of In is related to the presence of weakly bonded In ions.

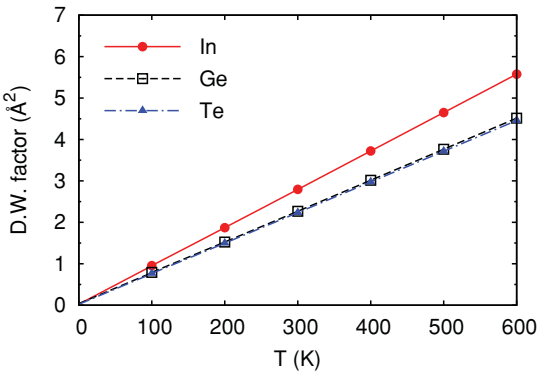

FIG. 20. (Color online) Debye-Waller factor B_κ (see text) of In, Ge, and Te atoms in a-IGT as a function of temperature.

IV. CONCLUSIONS

We have provided a model of the liquid and amorphous phases of $InGeTe_2$ by quenching from the melt within *ab initio* molecular dynamics simulations, similarly to what we reported previously for other phase change materials.[6,8,15,16] While the liquid is metallic, the amorphous phase is a semiconductor with a band gap of 0.5 eV. The local structure of a-IGT is similar to that of a-GST as concerns Ge and Te atoms. All Te and most Ge atoms are in a defective octahedral geometry ruled by the formation of p bonds, with Te mostly threefold coordinated and Ge mostly fourfold coordinated. A fraction of Ge atoms (13%, vs. 27% in a-GST[8]) is in a tetrahedral geometry promoted by the presence of wrong bonds (In-Ge and Ge-Ge). Phonons above 190 cm^{-1} are strongly localized on Ge tetrahedra as occurs in a-GST. Atoms of In are, instead, mostly fourfold coordinated in $InTe_4$ tetrahedra, similarly to the crystalline phase of InTe and In_2Te_5. As for GST and related binary systems, the local bonding geometry in the amorphous phase of IGT is mostly similar to the crystalline counterparts, which, however, in this case include cubic $InGeTe_2$ but also InTe and In_2Te_5 crystals. The higher crystallization temperature measured for a-IGT, which makes this system interesting for applications at high temperatures, might be the result of two concurring effects. On one hand, a crystallization temperature higher than in GST or GeTe is expected because of the higher melting point of IGT. On the other hand, if tetrahedra are absent in the crystalline cubic phase we might conceive that the large fraction of $InTe_4$ tetrahedra in a-IGT would hinder crystallization, resulting in a further increase in the crystallization temperature. This property might be shared with other phase change alloys containing In such as InSbTe.

ACKNOWLEDGMENTS

We thankfully acknowledge the computational resources provided by the DEISA Consortium under project PHASEALL and by the CSCS (Manno, CH). We acknowledge partial support from Italian MURST through project PRIN08. S.C. acknowledges support through the SNSF (Grant No. 200021-119882).

APPENDIX

TABLE III. Statistics of In, Ge, and Te coordination environments in a-IGT. The percentages of the total number of atoms of each element are given for configurations with a weight greater than 1%.

	1	2	3	4	5
In	4.9 Te: 4.1	7.8 Te_2: 4.3 GeTe: 3.3	9.8 $GeTe_2$: 5.9 Te_3: 2.2 Ge_2Te: 1.0	68.1 Te_4: 37.6 $InTe_3$: 14.5 $GeTe_3$: 10.2 Ge_2Te_2: 3.3 $GeInTe_2$: 2.0	7.9 Te_5: 2.9 $GeTe_4$: 1.8 Ge_3Te_2: 1.5
Ge			41.6 Te_3: 34.9 $GeTe_2$: 4.0 $InTe_2$: 2.6	48.3 Te_4: 15.0 $InTe_3$: 14.3 $GeTe_3$: 8.4 In_2Te_2: 6.1 $GeInTe_2$: 4.4	9.2 $InTe_4$: 3.5 $GeInTe_3$: 2.1 Te_5: 1.8
Te:		13.7 GeIn: 7.6 In_2: 4.0 Ge_2: 2.0	68.4 $GeIn_2$: 28.7 Ge_2In: 20.3 Ge_3: 11.6 In_3: 7.8	16.8 Ge_2In_2: 6.8 Ge_3In: 3.9 $GeIn_3$: 3.7 Ge_4: 1.3 In_4: 1.2	1.1

*marco.bernasconi@mater.unimib.it

[1] M. Wuttig and N. Yamada, Nat. Mater. **6**, 824 (2007).

[2] A. L. Lacaita and D. J. Wouters, Phys. Status Solidi A , **205**, 2281 (2008).

[3] A. Pirovano, A. L. Lacaita, A. Benvenuti, F. Pellizzer, and R. Bez, IEEE Trans. Electron Devices **51**, 452 (2004).

[4] T. Morikawa, K. Kurotsuchi, M. Kinoshita, M. Matsuzaki, Y. Matsui, Y. Fujisaki, S. Hanzawa, A. Kotabe, M. Terao, H. Moriya, T. Iwasaki, M. Matsuoka, F. Nitta, M. Moniwa, T. Koga, and N. Takaura, Electron Devices Meeting 2007, IEDM 2007, IEEE International (2007), pp. 307–310.

[5] K-H. Song, S.-C. Beak, and H.-Y. Lee, J. Appl. Phys. **100**, 024506 (2010).

[6] S. Caravati, M. Bernasconi, T. D. Kühne, M. Krack, and M. Parrinello, Appl. Phys. Lett. **91**, 171906 (2007).

[7] S. Caravati, M. Bernasconi, T. D. Kühne, M. Krack, and M. Parrinello, Phys. Rev. Lett. **102**, 205502 (2009).

[8] S. Caravati, M. Bernasconi, T. D. Kühne, M. Krack, and M. Parrinello, J. Phys. Condens. Matter **21**, 255501 (2009); **21**, 499803(E) (2009); **22**, 399801 (2010).

[9] J. Akola and R. O. Jones, Phys. Rev. B **76**, 235201 (2007); Phys. Rev. Lett. **100**, 205502 (2008).

[10] J. Akola and R. O. Jones, J. Phys. Condens. Matter **20**, 465103 (2008).

[11] J. Hegedus and S. R. Elliott, Nat. Mater. **7**, 399 (2008).

[12] J. Akola, R. O. Jones, S. Kohara, S. Kimura, K. Kobayashi, M. Takata, T. Matsunaga, R. Kojima, and N. Yamada, Phys. Rev. B **80**, 020201 (2009).

[13] J. Akola and R. O. Jones, Phys. Rev. Lett. **100**, 205502 (2008).

[14] Z. Sun, J. Zhou, A. Blomqvist, B. Johansson, and R. Ahuja, Appl. Phys. Lett. **93**, 061913 (2008).

[15] R. Mazzarello, S. Caravati, S. Angioletti-Uberti, M. Bernasconi, and M. Parrinello, Phys. Rev. Lett. **104**, 085503 (2010).

[16] S. Caravati, M. Bernasconi, and M. Parrinello, Phys. Rev. B **81**, 014201 (2010).

[17] T. D. Kühne, M. Krack, F. R. Mohamed, and M. Parrinello, Phys. Rev. Lett. **98**, 066401 (2007).

[18] The CP2K developers group [http://cp2k.berlios.de].

[19] J. VandeVondele, M. Krack, F. Mohamed, M. Parrinello, T. Chassaing, and J. Hutter, Comput. Phys. Commun. **167**, 103 (2005); M. Krack and M. Parrinello, in *High Performance Computing in Chemistry*, edited by J. Grotendorst, Vol. 25 (NIC, Zeuthen, 2004), pp. 29–51.

[20] J. P. Perdew, K. Burke, and M. Ernzerhof, Phys. Rev. Lett. **77**, 3865 (1996).

[21] S. Goedecker, M. Teter, and J. Hutter, Phys. Rev. B **54**, 1703 (1996); M. Krack, Theor. Chem. Acc. **114**, 145 (2005).

[22] [http://www.cpmd.org], Copyright IBM Corp 1990–2006, Copyright MPI für Festkörperforschung Stuttgart 1997–2001.

[23] J. Heyd, G. E. Scuseria, and M. Ernzerhof, J. Chem. Phys. **118**, 8207 (2003).

[24] M. I. Zargarova and M. M. Akperov, Izv. Akad. Auk. SSSR Neorg. Mater. **9**, 7 (1973).

[25] T. Matsunaga, N. Yamada, and Y. Kubota, Acta Crystallogr. B **60**, 685 (2004).

[26] Y. N. Nasirov, M. I. Zargarova, R. S. Gamidov, and M. M. Akperov, Izv. Akad. Auk. SSSR Neorg. Mater. **6**, 5 (1970).

[27] S. Grimme, J. Comput. Chem. **27**, 1787 (2006).

[28]D. A. Keen, J. Appl. Crystallogr. **34**, 172 (2001).
[29]C. Steimer, V. Coulet, W. Welnic, H. Dieker, R. Detemple, C. Bichara, B. Beuneu, J.-P. Gaspard, and M. Wuttig, Adv. Mater. **20**, 4535 (2008).
[30]S. R. Elliott, Nature **354**, 455 (1991); Phys. Rev. Lett. **67**, 711 (1991); P. S. Salmon, Proc. R. Soc. London A **445**, 351 (1994); C. Massobrio, M. Celino, and A. Pasquarello, Phys. Rev. B **70**, 174202 (2004).
[31]D. S. Franzblau, Phys. Rev. B **44**, 4925 (1991).
[32]J. H. C. Hogg and H. H. Sutherland, Acta Crystallogr. **32**, 2689 (1976).
[33]G. Henkelman, A. Arnaldsson, and H. Jonsson, Comp. Mater. Sci. **36**, 354 (2006).
[34]N. Marzari and D. Vanderbilt, Phys. Rev. B **56**, 12847 (1997).
[35]P. L. Silvestrelli, N. Marzari, D. Vanderbilt, and M. Parrinello, Solid State Commun. **107**, 7 (1998).
[36]J. Goldak, C. S. Barrett, D. Innes, and W. Youdelis, J. Chem. Phys. **44**, 3323 (1966).
[37]M. Xu, Y. Q. Cheng, H. W. Sheng, and E. Ma, Phys. Rev. Lett. **103**, 195502 (2009).
[38]K. Shportko, S. Kremers, M. Woda, D. Lencer, J. Robertson, and M. Wuttig, Nat. Mat. **7**, 653 (2008).
[39]B. Huang and J. Robertson, Phys. Rev. B **81**, 081204(R) (2010).
[40]K. S. Thygesen, L. B. Hansen, and K. W. Jacobsen, Phys. Rev. Lett. **94**, 026405 (2005).
[41]S. Caravati, M. Bernasconi, and M. Parrinello, J. Phys. Cond. Matt. **22**, 315801 (2010).
[42]H. H. Sutherland, J. H. C. Hogg, and P. D. Walton, Acta Crystallogr. **32**, 2539 (1976).
[43]K. Kastner, D. Adler, and H. Fritzshe, Phys. Rev. Lett. **37**, 1504 (1976).
[44]L.-M. Peng, S. L. Dudarev, and M. J. Whelan, *High Energy Electron Diffraction and Microscopy* (Oxford University Press, Oxfod 2004).